

AD

TECHNICAL REPORT ARCCB-TR-00003

**PRELIMINARY EROSION ANALYSIS FOR THE
EXPERIMENTAL M829E3 KINETIC ENERGY ROUND**

**S. SOPOK
R. LOOMIS
G. PFLEGL
C. RICKARD**

FEBRUARY 2000



**US ARMY ARMAMENT RESEARCH,
DEVELOPMENT AND ENGINEERING CENTER
CLOSE COMBAT ARMAMENTS CENTER
BENÉT LABORATORIES
WATERVLIET, N.Y. 12189-4050**



APPROVED FOR PUBLIC RELEASE; DISTRIBUTION UNLIMITED

20000306 092

DISCLAIMER

The findings in this report are not to be construed as an official Department of the Army position unless so designated by other authorized documents.

The use of trade name(s) and/or manufacturer(s) does not constitute an official endorsement or approval.

DESTRUCTION NOTICE

For classified documents, follow the procedures in DoD 5200.22-M, Industrial Security Manual, Section II-19, or DoD 5200.1-R, Information Security Program Regulation, Chapter IX.

For unclassified, limited documents, destroy by any method that will prevent disclosure of contents or reconstruction of the document.

For unclassified, unlimited documents, destroy when the report is no longer needed. Do not return it to the originator.

REPORT DOCUMENTATION PAGE			Form Approved OMB No. 0704-0188	
Public reporting burden for this collection of information is estimated to average 1 hour per response, including the time for reviewing instructions, searching existing data sources, gathering and maintaining the data needed, and completing and reviewing the collection of information. Send comments regarding this burden estimate or any other aspect of this collection of information, including suggestions for reducing this burden, to Washington Headquarters Services, Directorate for Information Operations and Reports, 1215 Jefferson Davis Highway, Suite 1204, Arlington, VA 22202-4302, and to the Office of Management and Budget, Paperwork Reduction Project (0704-0188), Washington, DC 20503.				
1. AGENCY USE ONLY (Leave blank)	2. REPORT DATE February 2000	3. REPORT TYPE AND DATES COVERED Final		
4. TITLE AND SUBTITLE PRELIMINARY EROSION ANALYSIS FOR THE EXPERIMENTAL M829E3 KINETIC ENERGY ROUND		5. FUNDING NUMBERS PRON No. J5850E52M21A		
6. AUTHOR(S) S. Sopok, R. Loomis (Picatinny Arsenal, Dover, NJ), G. Pflegl, and C. Rickard				
7. PERFORMING ORGANIZATION NAME(S) AND ADDRESS(ES) U.S. Army ARDEC Benet Laboratories, AMSTA-AR-CCB-O Watervliet, NY 12189-4050		8. PERFORMING ORGANIZATION REPORT NUMBER ARCCB-TR-00003		
9. SPONSORING/MONITORING AGENCY NAME(S) AND ADDRESS(ES) U.S. Army ARDEC Close Combat Armaments Center Picatinny Arsenal, NJ 07806-5000		10. SPONSORING/MONITORING AGENCY REPORT NUMBER		
11. SUPPLEMENTARY NOTES Presented at the 36 th JANNAF Combustion Meeting, NASA Kennedy Space Center, FL, 17-22 October 1999. Published in proceedings of the meeting.				
12a. DISTRIBUTION/AVAILABILITY STATEMENT Approved for public release; distribution unlimited.		12b. DISTRIBUTION CODE		
13. ABSTRACT (Maximum 200 words) The preliminary experimental 120-mm M829E3 kinetic energy round data described here represent a stage in the development cycle that occurred about a half year to a year ago. The computational erosion predictions are guided and supported by substantial field and laboratory data, including data from firing tests, laboratory tests, and nondestructive/destructive cannon erosion characterizations. This information is intended to provide a "snapshot" of development for that period, and is not directly related to the future type-classified M829E3 kinetic energy round. During that period, these modeling predictions put the program about 40 rounds shy of its required 180-round minimum program target, so further round optimization will likely contribute to the achievement of this goal. Further round optimizations will likely include changes in the weight and configuration of the propellant, projectile, case, and possible ablative. Results of this erosion analysis, erosion effective full charge factor analysis, and comparisons to the round's advanced type-classified counterpart are provided for the preliminary experimental M829E3 kinetic energy round used in the 120-mm M256 cannon at multiple round-conditioning temperatures. The computational method consisted of using our Unified Cannon Erosion Code. Differences exist between the preliminary experimental M829E3 kinetic energy round and its advanced type-classified counterpart including increased propellant weight, increased projectile weight, and RPD380 propellant instead of JA2 propellant. The preliminary experimental M829E3 kinetic energy round erosion analysis achieves erosion condemnation in a lesser number of rounds, and the worst eroded region has moved slightly more than a half meter up-bore compared to its advanced type-classified counterpart.				
14. SUBJECT TERMS Cannon Erosion Analysis, Experimental M829E3 Kinetic Energy Round		15. NUMBER OF PAGES 17		
		16. PRICE CODE		
17. SECURITY CLASSIFICATION OF REPORT UNCLASSIFIED	18. SECURITY CLASSIFICATION OF THIS PAGE UNCLASSIFIED	19. SECURITY CLASSIFICATION OF ABSTRACT UNCLASSIFIED	20. LIMITATION OF ABSTRACT UL	

TABLE OF CONTENTS

	<u>Page</u>
INTRODUCTION.....	1
COMPUTATIONAL AND EXPERIMENTAL METHODS	1
RESULTS AND DISCUSSION.....	2
REFERENCES.....	9

LIST OF ILLUSTRATIONS

1.	M829E3 NOVA gas pressure analysis	10
2.	M829E3 NOVA gas temperature analysis	10
3.	M829E3 MABL recovery enthalpy	11
4.	M829E3 MABL cold wall heat flux.....	11
5.	M829E3 CCET gas/wall thermochemistry	12
6.	M829E3 M256 subsurface exposure.....	12
7.	M829E3 enabling step in the erosion process for M256 cannon at 1.6 meters from RFT	13
8.	M829E3 accelerating step in the erosion process for M256 cannon at 1.6 meters from RFT	13
9.	M829E3 MACE HC chromium surface temperature analysis	14
10.	M829E3 MACE A723 interface temperature analysis.....	14
11.	M829E3 MACE A723 surface temperature analysis	15
12.	M829E3 MACE erosion onset	15
13.	M829E3 MACE erosion condemnation.....	16
14.	M829E3 MACE erosion summary.....	16

INTRODUCTION

In the early 1990s, the M829A2 kinetic energy round was type-classified for the 120-mm M256 tank cannon to defeat an improved armor not present in the Gulf War. This round served the U.S. Army well for the remainder of the 1990s, even though by 1995 there was an increased threat on the horizon. To meet this increased threat, the U.S. Army began developing a more advanced M829E3 kinetic energy round for the 120-mm M256 tank cannon to defeat the new advanced armor. Differences existing between the M829E3 kinetic energy round and its advanced type-classified counterpart include increased propellant weight, increased projectile weight, and use of RPD380 propellant instead of JA2 propellant.

Due to decreasing Department of Defense (DoD) dollars for weapons programs and the advancement of computational models that can represent these weapon systems, DoD has mandated that in some instances computational modeling may be substituted for field testing in order to save some of the limited weapon system dollars.

A unified computer model for predicting thermal-chemical-mechanical erosion in cannons was first described by Dunn et al. (ref 1) in 1995. This Unified Cannon Erosion Code is comprised of a collection of codes for predicting thermal-chemical-mechanical erosion in cannons. The computational erosion predictions are guided and supported by substantial field and laboratory data, including data from firing tests, laboratory tests, and nondestructive/destructive cannon erosion characterizations. The modeling effort has successfully predicted erosion for a number of high-profile Army and Navy weapon system programs.

Results of this erosion analysis, erosion effective full charge (EFC) factor analysis, and comparisons to the round's advanced type-classified counterpart are provided for the preliminary experimental M829E3 kinetic energy round used in the 120-mm M256 cannon at multiple round-conditioning temperatures.

COMPUTATIONAL AND EXPERIMENTAL METHODS

The Unified Cannon Erosion Code is comprised of a collection of codes for predicting thermal-chemical-mechanical erosion in cannons. This collection of codes is used here to analyze interior ballistics, boundary layer, thermochemistry, and thermal and erosion characteristics for the preliminary experimental M829E3 kinetic energy round used in the 120-mm M256 cannon at selected round-conditioning temperatures and axial positions. Experimental firing and laboratory data are used to guide, support, and calibrate these nonlinear analyses. References 1 and 2 provide a detailed description and the latest improvements to the Unified Cannon Erosion Code, which, in turn, includes the following interactive code modules:

- Standard interior ballistics gun code (XNOVAKTC)
- Standard heat transfer modified by mass addition to boundary layer rocket code modified for guns (MABL)

- Standard nonideal gas/wall thermochemical rocket code modified for guns (CCET)
- Standard wall material ablation conduction erosion rocket code modified for guns (MACE)

The XNOVAKTC interior ballistics code (refs 1-3) calculates the time-dependent core flow field characteristics for the 17.3-foot, 120-mm M256 cannon and its preliminary experimental M829E3 kinetic energy round. The RPD380 propellant charge weight is about 19 pounds without ablative and consists of approximately 59% nitrocellulose, 25% nitroglycerine, 15% diethylene glycol dinitrate, and 1% other minor species. Its igniter consists of 25 grams black powder and 25 grams CBI. Details relating to a medium-weight projectile are classified. This interior ballistics analysis interacts with the boundary layer analysis and thermochemistry analysis. Validation of this code is based on its calibration with actual pressure gauge and radar data.

The MABL cannon code (refs 1,2) is based on previous rocket codes (refs 4,5) and calculates boundary layer characteristics for the above interior ballistics cases. This boundary layer analysis interacts with the interior ballistics analysis, thermochemistry, and thermal/erosion analysis. Validation of this code is based on its calibration with actual subsurface metallographic and thermocouple data.

The CCET cannon code (refs 1,2,6) is based on previous rocket and cannon codes (refs 7,8) and calculates gas and gas/wall thermochemistry characteristics for the above interior ballistics cases. This thermochemistry analysis interacts with the interior ballistics analysis, boundary layer analysis, and thermal/erosion analysis. Validation of this code and product omissions are based on calibration with actual gas and gas/wall kinetic reaction rate data.

The MACE cannon code (refs 1,2) is based on a previous rocket code (ref 9) and calculates thermal and erosion characteristics, including wall temperature profiles and wall erosion profiles for the above interior ballistics cases. This thermal/erosion analysis interacts with the boundary layer analysis and thermochemistry analysis. Validation of this code is based on its calibration with actual subsurface metallographic data, thermocouple data, and borescope data.

RESULTS AND DISCUSSION

The preliminary experimental M829E3 kinetic energy round data described here represent a stage in the development cycle that occurred about a half year to a year ago. The computational predictions are guided and supported by substantial experimental firing and laboratory data. This information is intended to provide a "snapshot" of development for that period, and is not directly related to the future type-classified M829E3 kinetic energy round.

Figures 1 and 2 summarize the preliminary experimental M829E3 kinetic energy round XNOVAKTC interior ballistics analysis data for respective maximum values of gas pressure (P_g) and gas temperature (T_g) as a function of selected axial positions at selected round-conditioning temperatures. Gas velocity is omitted due to its classified nature. Maximum values were used instead of time-dependent data to simplify the appearance of these figures. Selected axial positions included 0.6, 1.6, 2.2, 3.3, and 5.1 meters from the rear face of the tube (RFT), while the selected round-conditioning included the hot (49°C), ambient (21°C), and cold (-31°C) temperatures. These five selected axial positions and three selected round-conditioning temperatures were used exclusively throughout the rest of this report. Experimental pressure-time and muzzle velocity data were used to calibrate this interior ballistics analysis. These M829E3 P_g and T_g values decrease with increasing axial position. These M829E3 P_g and T_g values also are up to 10% and 6%, respectively, higher than their M829A2 counterparts (ref 2).

Figures 3 and 4 summarize the preliminary experimental M829E3 kinetic energy round MABL boundary layer analysis data for respective maximum values of recovery enthalpy (H_r) and cold wall heat flux (Q_{cw}) as a function of the five selected axial positions at the three selected round-conditioning temperatures. Maximum values were again used instead of time-dependent data to simplify the appearance of these figures. Experimental chromium recrystallization depth, gun steel transformation depth, and thermocouple data were used to calibrate this boundary layer analysis. The H_r and Q_{cw} values increase with increasing axial position for the 0.6 to 1.2-meter from RFT region, both values peak in the 1.2 to 2.4-meter from RFT range, then both values decrease with increasing axial position to the muzzle. This heat transfer pattern from the boundary layer analysis significantly differs from the interior ballistics core flow pattern above, due to 1600°K combustion case gas cooling effects and turbulent gas mixing/heating effects. Additionally, both of these M829E3 values peak at about 1.6 meters from RFT, while their M829A2 counterparts peak at about 2.2 meters from RFT. The highest heat transfer position for the M829E3 round has moved up-bore 0.6 meter. The M829E3 H_r and Q_{cw} values are up to 11% and 6%, respectively, higher than their M829A2 counterparts (ref 2).

Figure 5 summarizes the preliminary experimental M829E3 kinetic energy round CCET thermochemical analysis data for values of reacting gas/wall enthalpy (H_{gw}) and ablation potential (B_a) as a function of wall temperatures (T_{wall}) for the high contraction (HC) chromium plate/A723 gun steel wall materials. Mean values were used to simplify the appearance of this figure. Experimental kinetic rate function data and subsurface metallographic data were used to calibrate the thermochemical analysis and transform the chemical equilibrium analysis into a partial chemical kinetic analysis. Characterization of crack wall layers, interface wall layers, bore surface layers, subsurface void residues, and surface residues further guided gas/wall kinetics calibration. The M829E3 HC chromium maximum T_{wall} is about 1820°K, up to 10% higher than its M829A2 counterpart, below its passivating oxidation temperature at about 2000°K, well below its sulfidation temperature above 2130°K, and well below its melting point at about 2130°K, thus explaining its inertness. The M829E3 A723/iron maximum T_{wall} is about 1470°K, up to 5% higher than its M829A2 counterpart, well above its rapid expansive flaking oxidation temperature at about 1050°K, and above its sulfidation temperature at about 1270°K. Additionally, it is below its iron oxide melting point at about 1640°K, equal to its iron sulfide

melting point at about 1470°K, and well below its A723/iron melting point at about 1720°K. These factors combined explain its reactivity (ref 2).

Various data required to calibrate the M829E3 erosion model were collected from a 120-mm M256 cannon, SN3212. This cannon was condemned by erosion at 347 total rounds that included a mix of type-classified and experimental round types with a 1000°K flame temperature (T_f) range. These round types were fired semi-chronologically and included:

- 103 M829 ($T_f \sim 3450^\circ\text{K}$)
- 97 M829A2 ($T_f \sim 3450^\circ\text{K}$)
- 15 Primex IRAD ($T_f \sim 3450^\circ\text{K}$)
- 28 ATK IRAD ($T_f \sim 3500^\circ\text{K}$)
- 6 TPE Fastcore ($T_f \sim 3750^\circ\text{K}$)
- 83 M829E3/RPD380 ($T_f \sim 3650^\circ\text{K}$)
- 15 M865 warmers scattered throughout ($T_f \sim 2750^\circ\text{K}$)

From previous work (ref 10), estimates of equivalent ambient-conditioned M829E3 rounds were predicted for each of these groups of round types. The results respectively were 16, 25, 4, 7, 12, 83, and 2 for a total of 149 equivalent ambient-conditioned M829E3 rounds. Numerous scoring holes near the 1.6-meter from RFT position, some exceeding 6-mm depth, condemned this cannon due to erosion.

Figure 6 summarizes the preliminary experimental M829E3 kinetic energy round borescope analysis data from M256 cannon SN3212 for the A723 gun steel subsurface exposure as a function of the selected axial positions at various equivalent experimental ambient-conditioned M829E3 rounds fired. The equivalent M829E3 rounds were measured at 1, exponentially estimated at 75, exponentially estimated at 120, and measured at 149. These experimental borescope data were used to calibrate the M829E3 cannon erosion analysis. These experimental data were used as a substitute for data from a thermal-mechanical crack model that is yet to be developed. The data were collected from this M256 cannon before commissioning and after its condemnation by using a magnifying borescope with a calibrated scale to measure the crack exposure and chromium plate loss in a given area as a function of specified axial positions and round counts. Prior to firing, HC chromium plate has fine cracking and finite shrinkage due to the manufacturing process. With progressive firing, HC chromium plate shrinks, heat checks, its interface to its gun steel substrate degrades, and eventually it spalls chromium platelets. The measured subsurface exposure pattern of M256 cannon SN3212 with significant experimental M829E3 rounds agrees with the predicted M829E3 boundary layer heat transfer pattern above, where both sets of values rose to a 1.6-meter from RFT peak and decreased thereafter. This differs from the experimental subsurface exposure pattern of M256 cannon SN1988 with significant M829A2 rounds that rose to a 2.2-meter from RFT peak and decreased thereafter. The measured M829E3 percent maximum subsurface exposure at 1.6 meters from RFT exceeds its M829A2 counterpart at 2.2 meters from RFT, and this occurred in about one-third as many equivalent respective rounds (ref 2).

Included herein are two preliminary micrographs, Figures 7 and 8, from a scanning electron microscope. These figures illustrate the mechanisms responsible for the erosion of M256 cannon SN3212 by significant experimental M829E3 kinetic energy rounds. Although many axial locations were examined, the erosion significantly peaked at about the 1.6-meter from RFT position. Evidence will follow outlining the mechanisms leading to this severe erosion around the 1.6-meter position and why other axial locations were less eroded. The features illustrated in these micrographs occur over and over around this peak erosion position and to a lesser extent at less eroded positions. Our cannon characterization knowledge was used to guide the M829E3 erosion modeling effort. For each of these scanning electron microscope micrographs, a fully coupled electron probe microanalysis by energy dispersive x-ray fluorescence spectroscopy was used to provide chemical analysis of important subsurface gun steel wall and interface layer regions on these micrographs. Chromium plate thickness was about 130 μm or 0.130 mm.

Figure 7 shows a preliminary experimental 2000x micrograph of M256 cannon SN3212 at 1.6 meters from RFT. This figure features the enabling step in the erosion process. As previously theorized, the focus of the enabling step in the gun erosion mechanism involves initial fine chromium plate cracks that provide a propellant gas mass transport path, which initializes gun steel degradation at the chromium/gun steel interface leading to gun erosion (ref 1). Early in an M256 cannon's life, due to the manufacturing process, its HC chromium plate has many fine cracks that extend from the chromium surface to the chromium/gun steel interface (ref 1). Clearly, the chromium/gun steel interface is degrading, which will eventually lead to chromium platelet spallation as interface damage links up from adjacent cracks. These cracks in the chromium are so fine and the interface damage so miniscule that they are not even visible at typical characterization magnifications of 100x. The very narrow width of these cracks prevents solid debris from arriving from the bore surface, thus restricting the contents of this gun steel void to combustion gas/gun wall products. Combustion gases travel down the narrow chromium cracks to the main gun steel voids and narrower interface gun steel voids by a high gas pressure filling mechanism, where they condense onto, adsorb onto, diffuse into, and/or react with the gun steel.

Increasing the magnification up to 30,000x allowed the imaging and analyzation of crack and interface wall layers on the gun steel by a fully coupled electron probe microanalysis technique. Carburized gun steel white layer and heat-affected zone are minimal under these crack and interface wall layers, probably due to the modest mass transport conditions. The crack and interface wall layer chemistries included iron, nickel, and chromium, which are major detectable elements of gun steel and partially compose these semi-metallic layers. In addition, the semi-metallic layers included measurable concentrations of oxygen from the propellant gas and sulfur from the igniter gas. Measurable concentrations of oxygen and sulfur in these gun steel layers are indicative of oxidation and sulfidation of iron, possibly nickel and possibly chromium from the gun steel, and possibly chromium from the chromium plate, as indicated by Natesan (ref 11).

Figure 8 shows a preliminary experimental 1000x micrograph of M256 cannon SN3212 at 1.6 meters from RFT featuring the accelerating step in the erosion process. Also, as previously theorized, the focus of this accelerating step in the gun erosion mechanism involves wider chromium cracks that are due to chromium shrinkage and increase the propellant gas mass transport path that accelerates gun steel degradation at the chromium/gun steel interface leading to gun erosion (ref 1). Toward the middle of an M256 cannon's life, its HC chromium plate heat checks/shrinks leading to advanced interface degradation, eventual chromium platelet spallation as interface damage links up from adjacent cracks, and subsequent bare gun steel gas wash (ref 1). The gun steel at the chromium/gun steel interface is more susceptible to interface degradation than either of its components separately due to its higher energy state and reactivity (ref 1). Oxidation and sulfidation (both oxidation types) of the gun steel wall iron can occur in a moderately-reduced combustion gas environment, since oxygen and sulfur have more of an affinity for this iron metal than they do for partially oxidized gas species (ref 1). Clearly, the chromium/gun steel interface degrades to a point where spallation of the center chromium platelet is inevitable, as interface damage links up from the two adjacent cracks. These cracks in the chromium and the interface damage are very visible at typical characterization magnifications of 100x. The wide width of these cracks allows solid debris from the surface to mix with combustion gas/gun wall products in this large gun steel void. Combustion gases travel down the wider chromium cracks to the main gun steel voids and narrower interface gun steel voids by an initial high gas pressure filling mechanism, followed by a turbulent convective mixing mechanism where they condense onto, adsorb onto, diffuse into, and/or react with the gun steel.

Increasing the magnification up to only 5000x allowed the imaging of crack wall layers on the gun steel. Increasing the magnification up to 50,000x allowed imaging and analyzation of the interface wall layers on the gun steel by a fully coupled electron probe microanalysis technique. Carburized gun steel white layer and heat-affected zone are now quite noticeable under these crack and interface wall layers due to the substantial mass transport conditions. As above, the crack and interface wall layer chemistries included iron, nickel, and chromium, which are major detectable elements of gun steel and partially compose these semi-metallic layers. These semi-metallic layers now included significant concentrations of oxygen from the propellant gas and sulfur from the igniter gas. Significant concentrations of oxygen and sulfur in these gun steel layers are indicative of oxidation and sulfidation of iron, possibly nickel and possibly chromium from the gun steel, and possibly chromium from the chromium plate, as indicated by Natesan (ref 11). In addition, these crack wall layers/surfaces included measurable concentrations of potassium from the igniter gas, as well as magnesium and silicon from the combustible case gas. The last three elements may have entered into the large gun steel void as a condensed species or as debris.

For M256 cannon SN3212, why does the 1.6-meter from RFT axial position have the peak erosion and not the onset of the chromium plated bore at 0.6 meter from RFT? Compared to the 1.6-meter from RFT position, the 0.6-meter from RFT position has less erosion due to a combination of factors. These include higher maximum gas pressure, deeper maximum crack depths into the gun steel, lower gas velocity, reduced turbulence, higher core gas temperature, and lower boundary layer gas temperature due to the much cooler added combustion case gas. These factors cumulatively result in reduced heat transferred to the wall. The maximum eroded

position and the maximum crack depth position tend not to correlate for tank cannons with combustible cases.

For M256 cannon SN3212, why does the 1.6-meter from RFT axial position have the peak erosion and not further down the bore at 2.2 meters from RFT? Compared to the 1.6-meter from RFT position, the 2.2-meter from RFT position also has less erosion again due to a combination of factors. These include lower maximum gas pressure, shallower maximum crack depths into the gun steel, higher gas velocity, increased turbulence, and lower gas temperature. These factors cumulatively result in reduced heat transferred to the wall.

Figure 9 summarizes the preliminary experimental M829E3 kinetic energy round MACE wall temperature profile analysis data for values of HC chromium maximum surface temperature (T_{wall}) as a function of the selected axial positions at the selected round-conditioning temperatures. The M829E3 HC chromium maximum T_{wall} is about 1820°K, up to 10% higher than its M829A2 counterpart, below its passivating oxidation temperature at about 2000°K, well below its sulfidation temperature above 2130°K, and well below its melting point at about 2130°K, thus explaining its inertness (ref 2).

Figure 10 summarizes the preliminary experimental M829E3 kinetic energy round MACE wall temperature profile analysis data for values of A723 maximum interface wall temperature (T_{wall}) as a function of the selected axial positions at the selected round-conditioning temperatures. These T_{wall} values are a combination of conduction and convection at the crack and interface walls. The M829E3 A723/iron maximum T_{wall} is about 1290°K, up to 5% higher than its M829A2 counterpart, well above its rapid expansive flaking oxidation temperature at about 1050°K, and above its sulfidation temperature at about 1270°K. Additionally, it is below its iron oxide melting point at about 1640°K, below its iron sulfide melting point at about 1470°K, and well below its A723/iron melting point at about 1720°K. These factors combined explain its reactivity (ref 2). Diffusion, reactions, transformations, and gas wash thermochemically degrade interfacial gun steel through cracks in the chromium plate.

Figure 11 summarizes the preliminary experimental M829E3 kinetic energy round MACE wall temperature profile analysis data for values of A723 maximum surface minus 0.13-mm wall temperature (T_{wall}) as a function of the selected axial positions at the selected round-conditioning temperatures. The M829E3 A723/iron maximum T_{wall} is about 1470°K, up to 5% higher than its M829A2 counterpart, well above its rapid expansive flaking oxidation temperature at about 1050°K, and above its sulfidation temperature at about 1270°K. Additionally, it is below its iron oxide melting point at about 1640°K, equal to its iron sulfide melting point at about 1470°K, and well below its A723/iron melting point at about 1720°K. These factors combined explain its reactivity (ref 2). Diffusion, reactions, transformations, and gas wash thermochemically degrade surface gun steel.

Preliminary experimental M829E3 kinetic energy round MACE wall temperature profile analysis data in Figures 9 through 11 correlate with the predicted M829E3 boundary layer heat transfer pattern above, where values rose to a 1.6-meter from RFT peak and decreased thereafter. This differs from its M829A2 counterpart, which rose to a 2.2-meter from RFT peak and

decreased thereafter (ref 2). In these three figures, maximum values were used instead of time-dependent data to simplify their appearance. Also in these three figures, experimental chromium recrystallization depth, gun steel transformation depth, and thermocouple data were used to calibrate the predicted wall temperature profiles.

Figures 12 and 13 summarize the preliminary experimental M829E3 kinetic energy round MACE cumulative erosion analysis data for respective values of cumulative rounds to 0.13-mm erosion (gun steel gas wash onset) and 5-mm erosion (gun steel erosion condemnation) as a function of the selected axial positions at the three selected round-conditioning temperatures and at an equal distribution of these three conditioning temperatures. For these figures, cumulative rounds to 0.13-mm gun steel gas wash onset and 5-mm gun steel erosion condemnation both inversely correlate with the predicted M829E3 boundary layer heat transfer pattern above where values decreased to a 1.6-meter from RFT minimum and increased thereafter. The values in these two figures occurred about a factor of 3.3 times sooner than their M829A2 counterparts. These counterparts had a different peak eroded position, which decreased to a 2.2-meter from RFT minimum and increased thereafter (ref 2). The preliminary experimental M829E3 kinetic energy round erosion analysis achieved erosion condemnation in a lesser number of rounds with the worst eroded region moving slightly more than a half meter up-bore compared to its M829A2 counterpart.

Figure 14 summarizes the preliminary experimental M829E3 kinetic energy round MACE cumulative erosion analysis data for values of cumulative rounds at the 1.6-meter from RFT position as a function of cumulative erosion at the three selected round-conditioning temperatures and at an equal distribution of these three conditioning temperatures. This figure is provided to further summarize the peak eroded 1.6-meter from RFT position, which governs erosion condemnation. For the respective 49°C, 21°C, -32°C, and equal distribution cases at this position, achievement of the 0.13-mm gun steel gas wash onset depth was at about 30, 50, 70, and 40 rounds, while achievement of the 5-mm gun steel erosion condemnation depth was at about 100, 160, 230, and 140 rounds.

Although it is not necessary to assign a set of erosion EFC factors until the M829E3 kinetic energy round is type-classified, a single estimated value is given. A preliminary experimental M829E3 kinetic energy round erosion EFC factor for the 21°C temperature condition is about three, based on its M829A2 counterpart at the 21°C temperature condition with a value of one (ref 10).

The preliminary experimental 120-mm M829E3 kinetic energy round data presented here represent a stage in the development cycle that occurred about a half year to a year ago. The computational predictions are guided and supported by substantial experimental firing and laboratory data. This information is intended to provide a "snapshot" of development for that period, and is not directly related to the future type-classified M829E3 kinetic energy round. During that period, these modeling predictions put the program about 40 rounds shy of its required 180-round minimum program target, so further round optimization will likely contribute to the achievement of this goal. Further round optimizations will likely include changes in the weight and configuration of the propellant, projectile, case, and possible ablative.

REFERENCES

1. Dunn, S., Sopok, S., Coats, D., O'Hara, P., Nickerson, G., and Pflegl, G., "Unified Computer Model for Predicting Thermochemical Erosion in Gun Barrels," *Proceedings of 31st AIAA Joint Propulsion Conference*, San Diego, CA, July 1995; Also *AIAA Journal of Propulsion and Power*, Volume 15, Number 4, pp. 601-612.
2. Sopok, S., Vottis, P., O'Hara, P., Pflegl, G., and Rickard, C., "Comprehensive Erosion Model for the 120-mm M256/M829A2 Gun System," *Proceedings of 120-mm International Joint Configuration Board Meeting*, Hampton, VA, May 1998.
3. Gough, P., "The XNOVAKTC Code," Paul Gough Associates, Portsmouth, NH, U.S. Army BRL-CR-627, February 1990.
4. Levine, J., "Transpiration and Film Cooling Boundary Layer Computer Program (MABL) - Numerical Solution of the Turbulent Boundary Layer Equations with Equilibrium Chemistry," NASA Marshall N72-19312, June 1971.
5. Nickerson, G., Berker, D., Coats, D., and Dunn, S., "Two-Dimensional Kinetics (TDK) Nozzle Performance Computer Program," Software and Engineering Associates, Inc., Carson City, NV, NASA Marshall NAS8-39048, March 1993.
6. Coats, D., and Dunn, S., "A New Chemical Equilibrium Code with Compressibility Effects," *Proceedings of the 33rd JANNAF Combustion Meeting*, Monterey, CA, October 1996.
7. Gordon, S., and McBride, B., "Computer Program for Calculation of Complex Chemical Equilibrium Compositions, Rocket Performance, Incident and Reflected Shocks, and Chapman-Jouguet Detonations (CET)," NASA SP-273, NASA Lewis Research Center, Cleveland, OH, March 1971.
8. Freedman, E., "BLAKE - A Thermodynamic Code Based on Tiger: User's Guide and Manual," Technical Report ARBRL-TR-02411, U.S. Army Ballistic Research Laboratory, Aberdeen Proving Ground, MD, July 1982.
9. Dunn, S., "Materials Ablation Conduction Erosion Program (MACE)," Software and Engineering Associates, Inc., Carson City, NV, June 1989.
10. Sopok, S., and Billington, R., "Erosion EFC Factors for Kinetic Energy Rounds Used in the 120-mm M256 Tank Cannon," *Proceedings of 35th AIAA Joint Propulsion Conference*, Los Angeles, CA, June 1999.
11. Natesan, K., "Corrosion-Erosion Behavior of Materials - Oxidation and Sulfidation of Metal Materials in Combustion Systems," *Proceedings of the Corrosion Resistant Metals and Oxidation Activity Meeting of the American Society for Metals*, St. Louis, MO, October 1978.

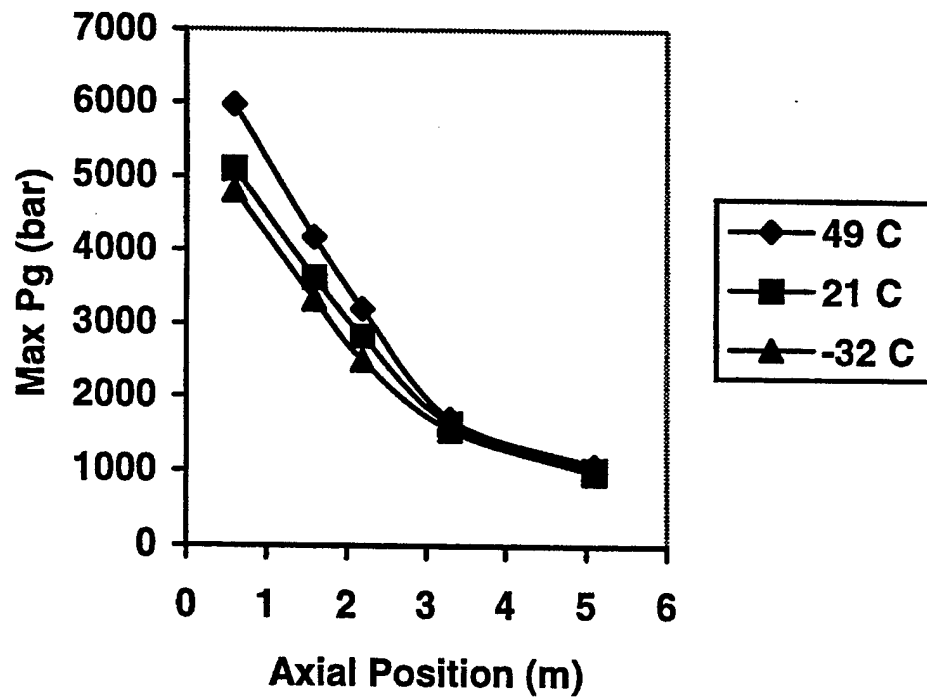


Figure 1. M829E3 NOVA gas pressure analysis.

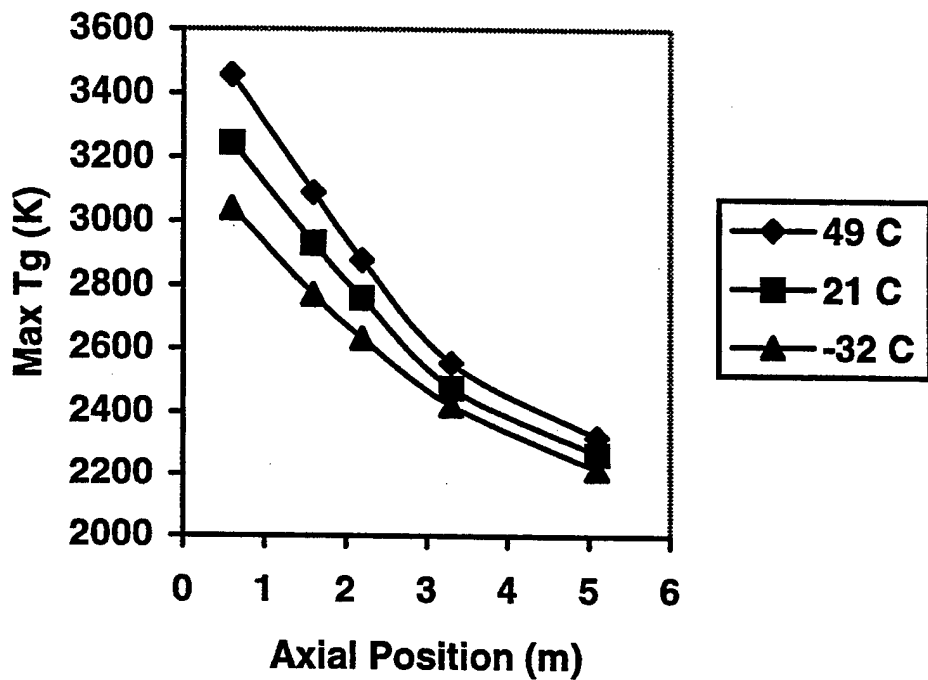


Figure 2. M829E3 NOVA gas temperature analysis.

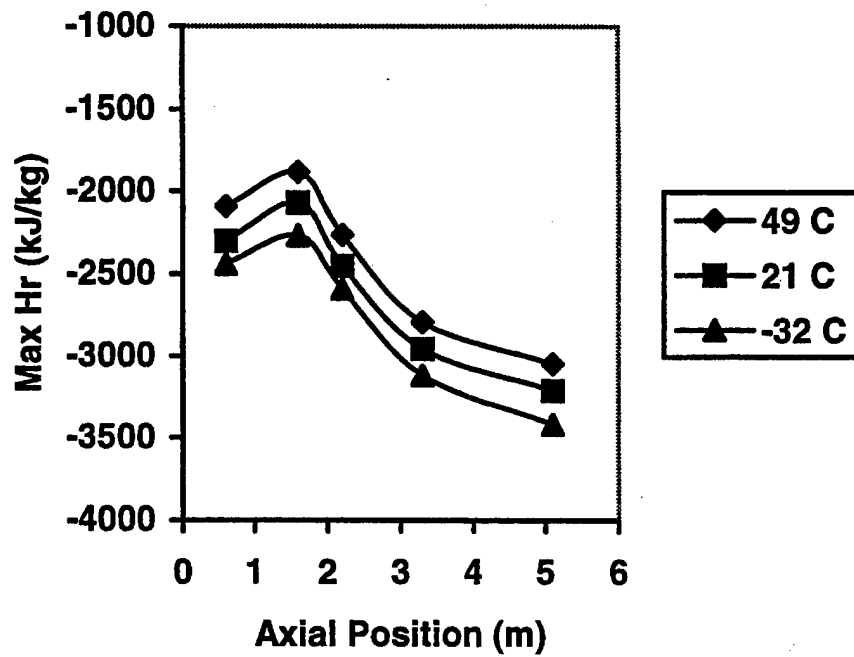


Figure 3. M829E3 MABL recovery enthalpy.

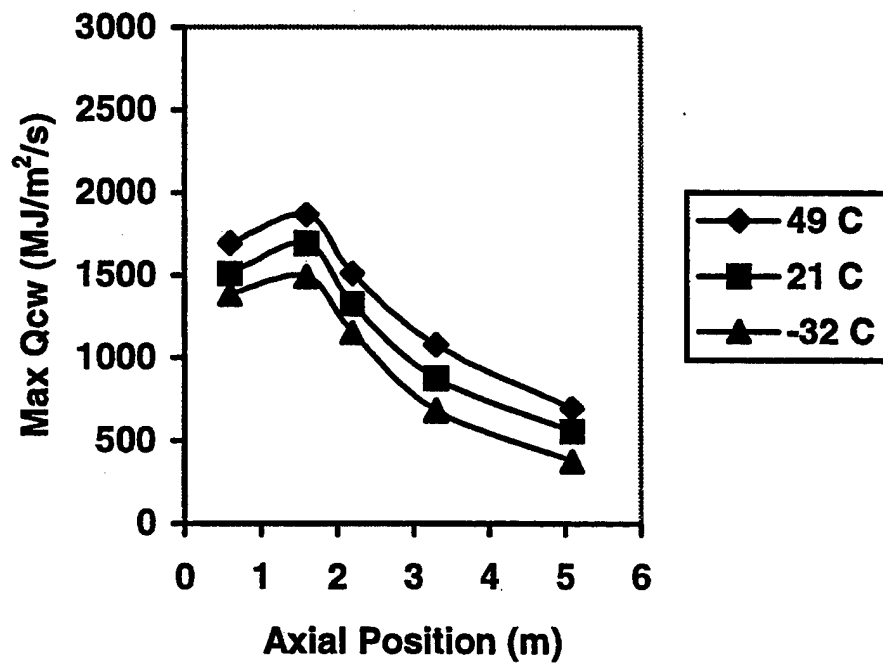


Figure 4. M829E3 MABL cold wall heat flux.

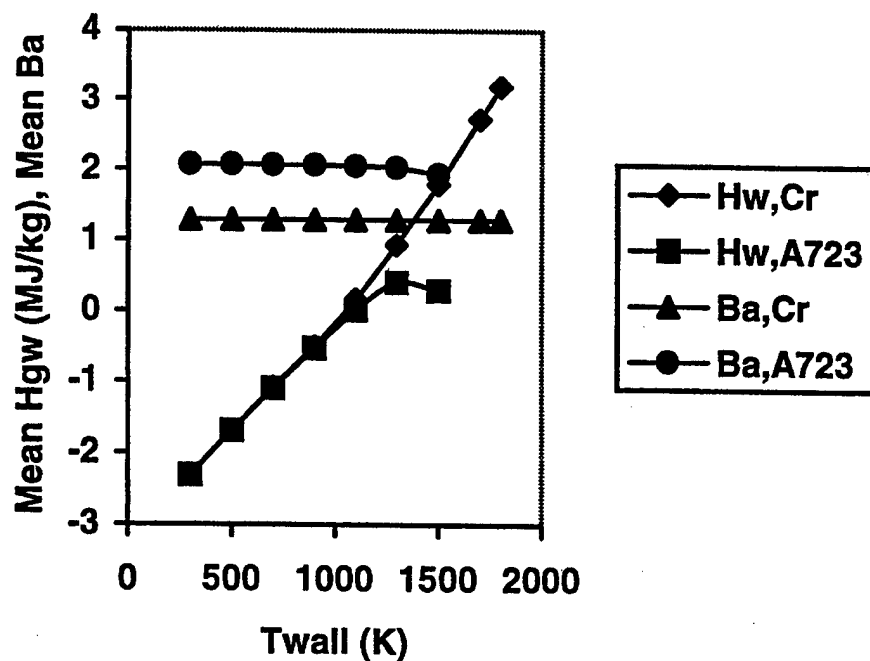


Figure 5. M829E3 CCET gas/wall thermochemistry.

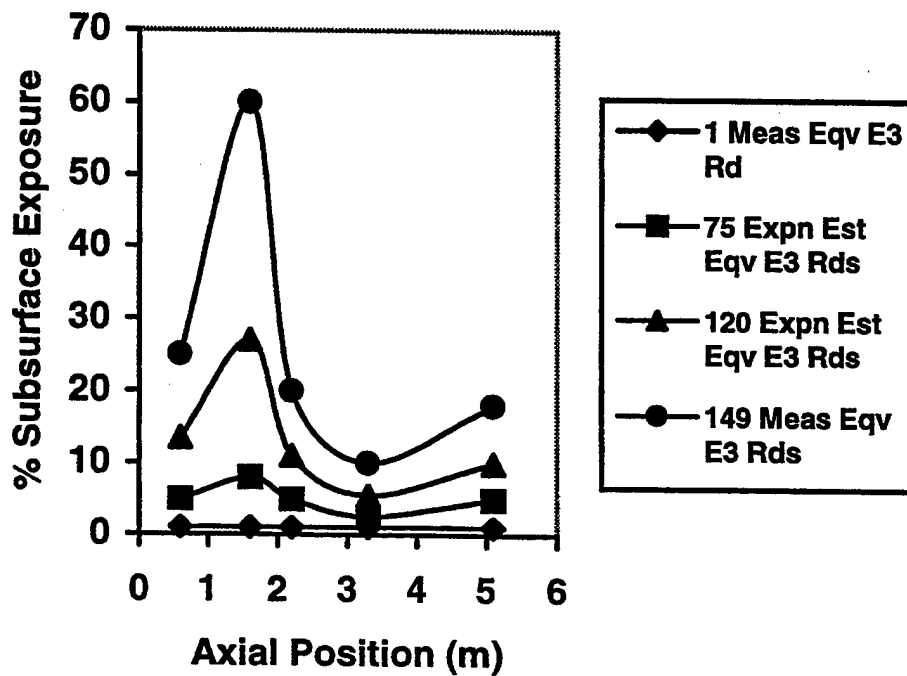


Figure 6. M829E3 M256 subsurface exposure.

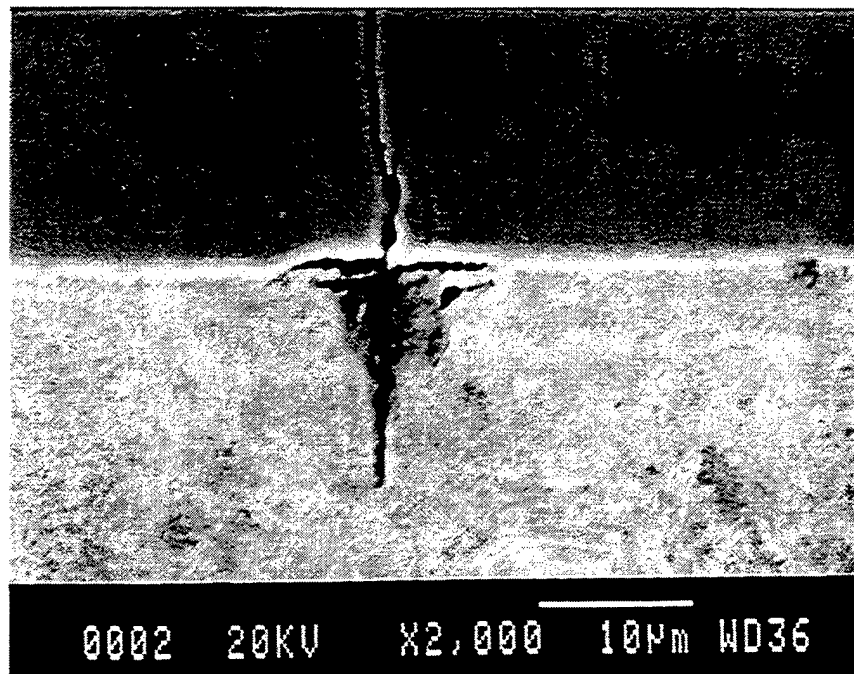


Figure 7. M829E3 enabling step in the erosion process for M256 cannon at 1.6 meters from RFT. (There is approximately 130 μm chromium plate (top) on a gun steel substrate (bottom).)

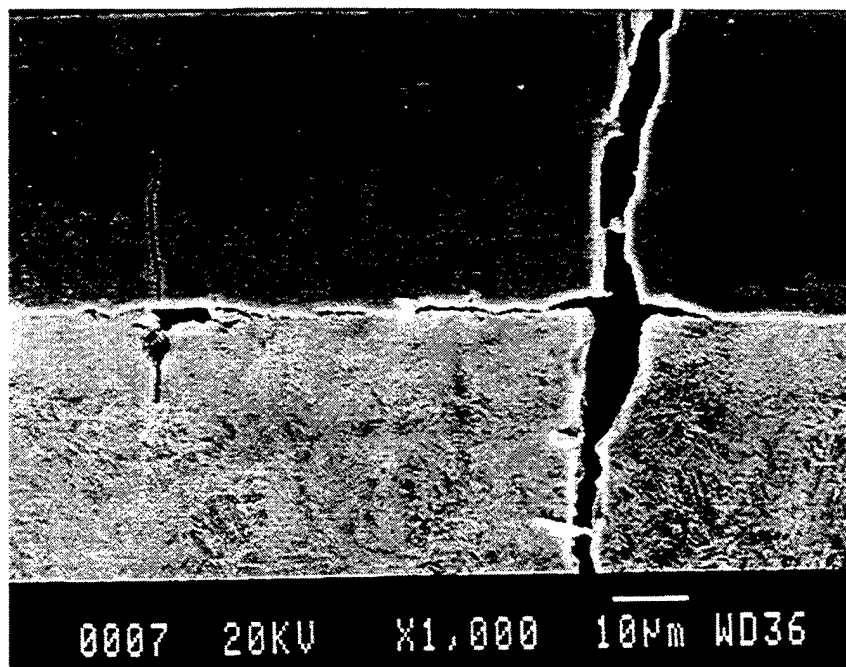


Figure 8. M829E3 accelerating step in the erosion process for M256 cannon at 1.6 meters from RFT. (There is approximately 130 μm chromium plate (top) on a gun steel substrate (bottom).)

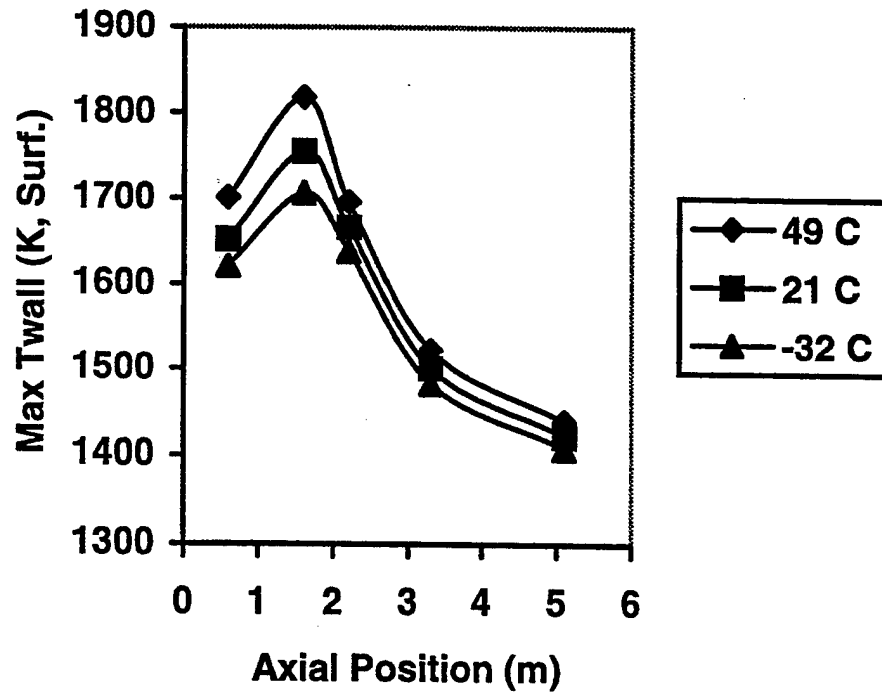


Figure 9. M829E3 MACE HC chromium surface temperature analysis.

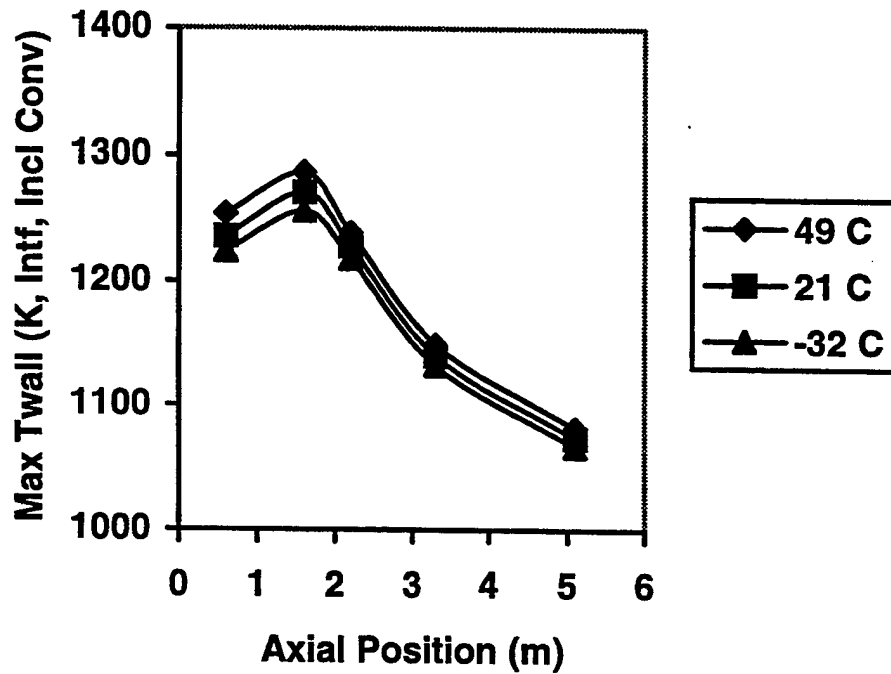


Figure 10. M829E3 MACE A723 interface temperature analysis.

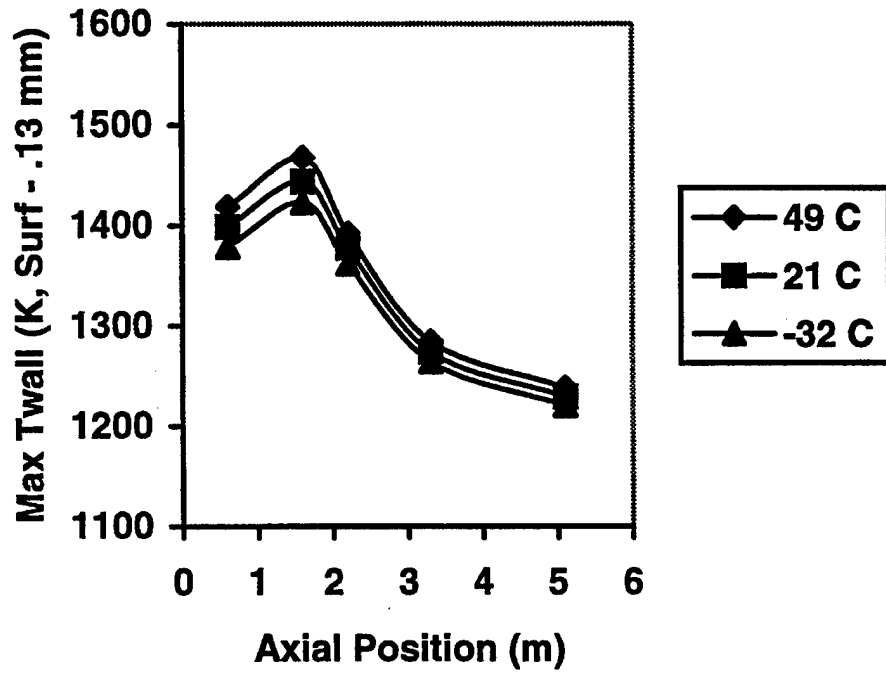


Figure 11. M829E3 MACE A723 surface temperature analysis.

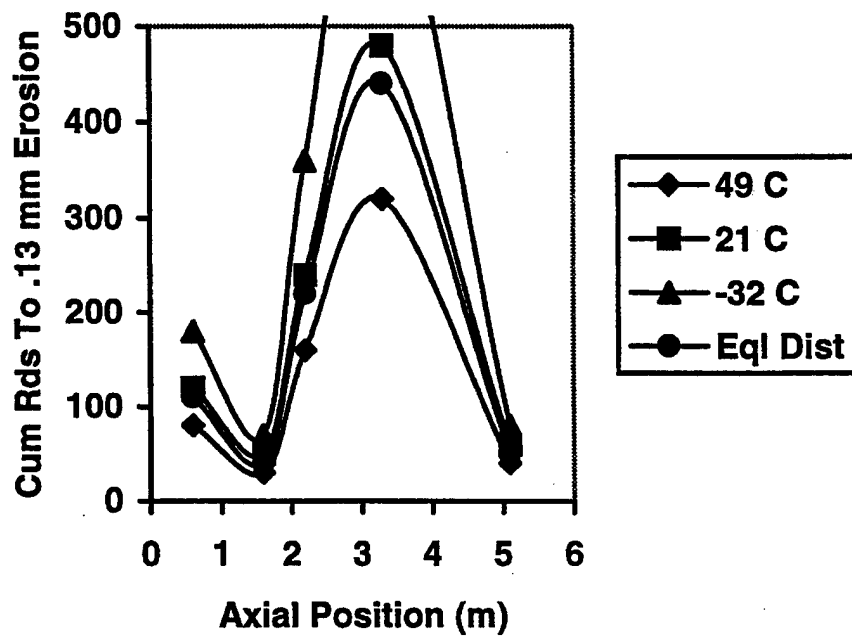


Figure 12. M829E3 MACE erosion onset.

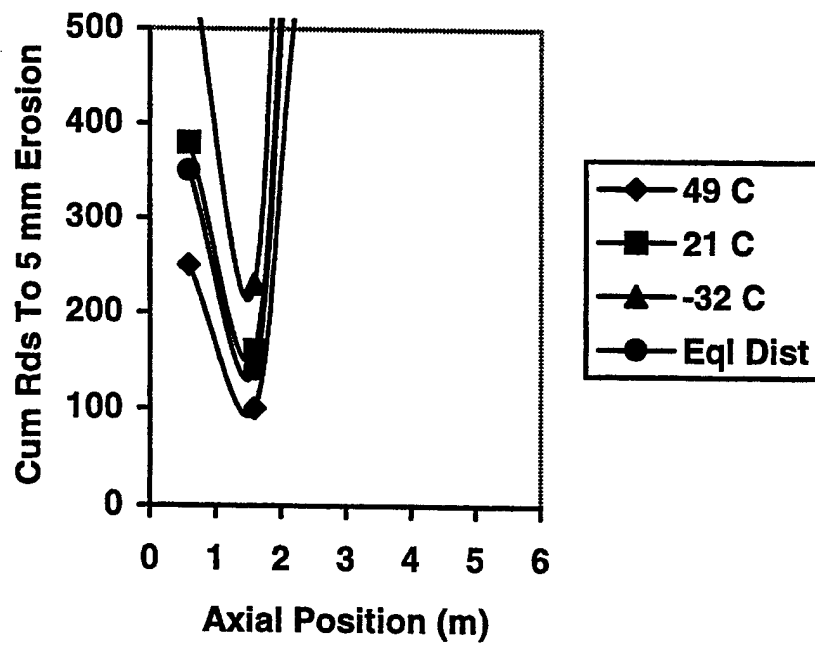


Figure 13. M829E3 MACE erosion condemnation.

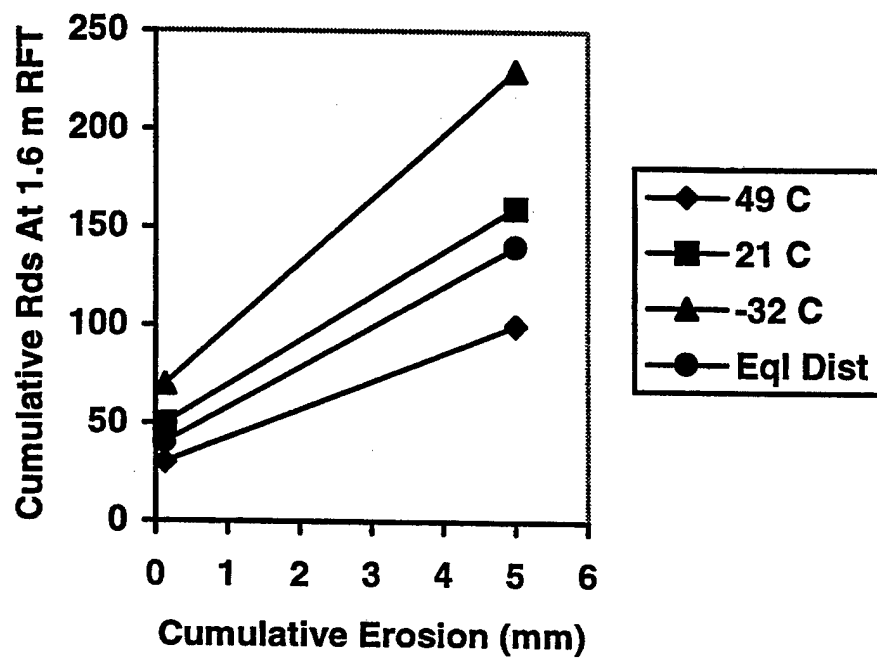


Figure 14. M829E3 MACE erosion summary.

TECHNICAL REPORT INTERNAL DISTRIBUTION LIST

	<u>NO. OF COPIES</u>
TECHNICAL LIBRARY ATTN: AMSTA-AR-CCB-O	5
TECHNICAL PUBLICATIONS & EDITING SECTION ATTN: AMSTA-AR-CCB-O	3
OPERATIONS DIRECTORATE ATTN: SIOWV-ODP-P	1
DIRECTOR, PROCUREMENT & CONTRACTING DIRECTORATE ATTN: SIOWV-PP	1
DIRECTOR, PRODUCT ASSURANCE & TEST DIRECTORATE ATTN: SIOWV-QA	1

NOTE: PLEASE NOTIFY DIRECTOR, BENÉT LABORATORIES, ATTN: AMSTA-AR-CCB-O OF ADDRESS CHANGES.

TECHNICAL REPORT EXTERNAL DISTRIBUTION LIST

	<u>NO. OF COPIES</u>		<u>NO. OF COPIES</u>
DEFENSE TECHNICAL INFO CENTER ATTN: DTIC-OCA (ACQUISITIONS) 8725 JOHN J. KINGMAN ROAD STE 0944 FT. BELVOIR, VA 22060-6218	2	COMMANDER ROCK ISLAND ARSENAL ATTN: SIORI-SEM-L ROCK ISLAND, IL 61299-5001	1
COMMANDER U.S. ARMY ARDEC ATTN: AMSTA-AR-WEE, BLDG. 3022 AMSTA-AR-AET-O, BLDG. 183 AMSTA-AR-FSA, BLDG. 61 AMSTA-AR-FSX AMSTA-AR-FSA-M, BLDG. 61 SO AMSTA-AR-WEL-TL, BLDG. 59 PICATINNY ARSENAL, NJ 07806-5000	1 1 1 1 1 2	COMMANDER U.S. ARMY TANK-AUTMV R&D COMMAND ATTN: AMSTA-DDL (TECH LIBRARY) WARREN, MI 48397-5000 COMMANDER U.S. MILITARY ACADEMY ATTN: DEPT OF CIVIL & MECH ENGR WEST POINT, NY 10966-1792	1 1
DIRECTOR U.S. ARMY RESEARCH LABORATORY ATTN: AMSRL-DD-T, BLDG. 305 ABERDEEN PROVING GROUND, MD 21005-5066	1	U.S. ARMY AVIATION AND MISSILE COM REDSTONE SCIENTIFIC INFO CENTER ATTN: AMSAM-RD-OB-R (DOCUMENTS) REDSTONE ARSENAL, AL 35898-5000	2
DIRECTOR U.S. ARMY RESEARCH LABORATORY ATTN: AMSRL-WM-MB (DR. B. BURNS) ABERDEEN PROVING GROUND, MD 21005-5066	1	COMMANDER U.S. ARMY FOREIGN SCI & TECH CENTER ATTN: DRXST-SD 220 7TH STREET, N.E. CHARLOTTESVILLE, VA 22901	1
COMMANDER U.S. ARMY RESEARCH OFFICE ATTN: TECHNICAL LIBRARIAN P.O. BOX 12211 4300 S. MIAMI BOULEVARD RESEARCH TRIANGLE PARK, NC 27709-2211	1		

NOTE: PLEASE NOTIFY COMMANDER, ARMAMENT RESEARCH, DEVELOPMENT, AND ENGINEERING CENTER,
BENÉT LABORATORIES, CCAC, U.S. ARMY TANK-AUTOMOTIVE AND ARMAMENTS COMMAND,
AMSTA-AR-CCB-O, WATERVLIET, NY 12189-4050 OF ADDRESS CHANGES.
